

This is the peer reviewed version of the following article: Yang, C., Wei, X., & Hao, J. (2018). Colossal permittivity in TiO₂ co-doped by donor Nb and isovalent Zr. Journal of the American Ceramic Society, 101(1), 307-315, which has been published in final form at <https://doi.org/10.1111/jace.15196>. This article may be used for non-commercial purposes in accordance with Wiley Terms and Conditions for Use of Self-Archived Versions. This article may not be enhanced, enriched or otherwise transformed into a derivative work, without express permission from Wiley or by statutory rights under applicable legislation. Copyright notices must not be removed, obscured or modified. The article must be linked to Wiley's version of record on Wiley Online Library and any embedding, framing or otherwise making available the article or pages thereof by third parties from platforms, services and websites other than Wiley Online Library must be prohibited.

Colossal permittivity in TiO₂ co-doped by donor Nb and isovalent Zr

Chao Yang¹, Xianhua Wei¹, Jianhua Hao²

¹ State Key Laboratory Cultivation Base for Nonmetal Composites and Functional Materials,

Southwest University of Science and Technology, Mianyang 621010, P. R. China

² Department of Applied Physics, The Hong Kong Polytechnic University, Hung Hom, Hong Kong,

P. R. China

Abstract

Effect of isovalent Zr dopant on the colossal permittivity (CP) properties was investigated in (Zr+Nb) co-doped rutile TiO₂ ceramics, i.e., Nb_{0.5%}Zr_xTi_{1-x}O₂. Compared with those of single Nb-doped TiO₂, the CP properties of co-doped samples showed better frequency stability with lower dielectric losses. Especially, a CP up to 6.4×10^4 and a relatively low dielectric loss (0.029) of $x = 2\%$ sample were obtained at 1 kHz and room temperature. Moreover, both dielectric permittivity and loss were nearly independent of direct current bias, and measuring temperature from room temperature to around 100 °C. Based on X-ray photoelectron spectroscopy, the formation of oxygen vacancies was suppressed due to the incorporation of Zr ions. Furthermore, it induced the enhancement of the conduction activation energy according to the impedance spectroscopy. The results will provide a new routine to achieve a low dielectric loss in the CP materials.

Keywords: Colossal permittivity, Doped TiO₂, Impedance spectroscopy, XPS

Correspondence

Xianhua Wei, State Key Laboratory Cultivation Base for Nonmetal Composites and Functional Materials, Southwest University of Science and Technology, Mianyang 621010, P. R. China

Email: weixianhua@swust.edu.cn

Jianhua Hao, Department of Applied Physics, The Hong Kong Polytechnic University, Hung

Hom, Hong Kong, P. R. China

Email: jh.hao@polyu.edu.hk

1. Introduction

Effects of doping elements on the dielectric properties of TiO_2 have received much attention since a new colossal permittivity (CP) material (In+Nb) co-doped rutile TiO_2 was reported by Hu et al.¹ Nb donor doping in this new CP material can raise the permittivity to values above 10^4 due to the creation of delocalized electrons by reducing Ti^{4+} to Ti^{3+} . Meanwhile, In acceptor doping has little or no effect on the permittivity but results in lower dielectric losses because it provides a local oxygen-deficient environment to hold back the delocalized electrons. Furthermore, it exhibits a largely temperature- and frequency-independent CP as well as a low dielectric loss, which is superior to those of other candidates for CP like ferroelectrics,² $\text{CaCu}_3\text{Ti}_4\text{O}_{12}$,^{3,4} doped NiO ,⁵ and $\text{La}_{15/8}\text{Sr}_{1/8}\text{NiO}_4$.⁶ Up to now, similar CP results have been reported in rutile TiO_2 ceramics by co-doping acceptor ions (trivalent ions: Al, Ga, In, or rare earth ions; bivalent ions: Zn, or alkaline earth ions) and donor elements (pentavalent ions: Nb or Ta).⁷⁻²¹ Most of those reports are convinced of the formation of electron-pinned defect-dipole (EPDD), while other mechanisms have also been proposed including interface effect arising from internal barrier layer capacitor (IBLC) effect,^{10,22} electrode effect,¹¹ hopping conductivity,²³ surface barrier layer effect²⁴ and microscopic inhomogeneities and polaronic relaxation.²⁵ It seems a prerequisite to achieve CP and low dielectric loss via the simultaneous incorporation of acceptor and donor substitutions into TiO_2 , although the mechanism is still controversial.

According to Hume-Rothery rule, a substitutional solid solution can be formed when the ionic radius of doped and host ions must differ less than 15%.²⁶ The pentavalent ions of Nb and Ta have a very close size to that of Ti ($r_{\text{Nb}} = r_{\text{Ta}} = 78$ pm, $r_{\text{Ti}} = 74.5$ pm). But the radii of most acceptor ions except Mg, Al, and Ga are beyond the range. It could easily induce the presence of secondary phases,

especially in the case of rare earth ions doped TiO₂ with a very large mismatch.^{7,8,14} Actually, an isovalent substitution of Ti by Zr has also been found to be an effective way to tune the dielectric properties of perovskite oxides including Curie temperature, permittivity and loss.^{27,28} Both Ti and Zr belong to group IVB, while the ionic radius of Zr ($r_{\text{Zr}} = 86$ pm, the mismatch of $r_{\text{Zr}}/r_{\text{Ti}} \sim 15\%$) is slightly larger than that of Ti. In addition, Zr possessing one more electron shell is beneficial to form the stronger combination to effectively localize the electron, which would favor lowering the dielectric loss. Moreover, Zr⁴⁺ is chemically more stable than Ti⁴⁺. Therefore, the oxygen ions are expected to be prevented from escaping the crystals. The conductivity caused by electron hopping between Ti⁴⁺ and Ti³⁺ could also be suppressed. Doping Zr into the CP CaCu₃Ti₄O₁₂ is reported to reduce the dielectric loss.²⁹ To date, the investigation on dielectric properties of co-doped TiO₂ with partially occupied by Zr ion is still absent. In this work, (Zr+Nb) co-doped TiO₂ ceramics are synthesized by solid-state sintering. Effects of doping content on microstructure, chemical composition, and dielectric properties are investigated.

2. Experimental procedure

Ceramics with a composition of Zr_xNb_{0.005}Ti_{0.995-x}O₂ ($x = 0\%, 0.5\%, 2\%, 5\%$) were prepared by using conventional solid-state reactions of rutile TiO₂ (99.99%), Nb₂O₅ (99.99%) and ZrO₂ (99.99%). The powders were weighted according to their stoichiometric composition and then fully grinded by ball-milling with zirconia balls for 8 h in ethanol to get the fine powders (mostly < 1 μm). The resultant slurries were dried and then calcined at 1000 °C for 4 h in air. After calcination, the samples were thoroughly reground and the dried powders incorporating a 5 wt% polyvinyl alcohol (PVA) binder solution were pressed into pellets with a diameter of around 10 mm and a thickness of 1.5 mm by uniaxial compression. These disk samples were fired at 650 °C for 6 h in air to remove the organic

PVA binder and then sintered at 1400 °C for 10 h in air, with a heating rate of 3 °C/min. The sintered samples were furnace-cooled to room temperature to obtain dense ceramic samples. The relative densities are 94.9%, 96.0%, 96.8%, and 98.5% for those ceramics with the doping constant of 0%, 0.5%, 2%, and 5%, according to the Archimedes' method. Besides, the sintered ceramics were fully polished and then pasted with silver on both sides. After that, the samples were annealed at 730 °C for 15 mins in air. X-ray diffraction (XRD) with Cu K α ($\lambda = 0.154$ nm) radiation (DMAX1400, Rigaku) was used to characterize the phase structures of the ceramics. Raman spectra had been recorded with an InVia Renishaw microscope by using the 514 nm laser line. The surface morphologies, and elemental mapping of the samples were performed by scanning electron microscopy (SEM) (MAIA3, Tescan). The valence states of elements in the ceramics were analyzed by X-ray photoelectron spectroscopy (XPS) on the system of a Thermo SCIENTIFIC ESCALAB 250Xi. A monochromatic aluminium K α radiation source with energy of 1486.8 eV was used in the system. The frequency dependence of dielectric properties was measured by an impedance analyzer (HP 4294A, Agilent) over the range of 10^2 to 10^6 Hz. The temperature dependence of the dielectric properties was measured by a LCR meter (Agilent E4980A, Agilent) which was equipped with a temperature-controlled probe stage (Linkam TS1500E, Linkam Scientific Instruments Ltd).

3. Results and discussion

Fig. 1(a) shows the XRD patterns of the $Zr_xNb_{0.005}Ti_{0.995-x}O_2$ samples sintered at 1400 °C for 10 h in air. All diffraction peaks of the ceramics were indexed as pure rutile phase according to (JCPDS 21-1276) at different doping contents of (Zr+Nb), without any intermediate phases as shown in Fig. 1(b). It is easily explained by the ZrO_2 - TiO_2 phase diagram that pure rutile phase can be formed for the doping level under 5% ZrO_2 , at the sintering temperature of 1400 °C.^{30,31} Besides, Zr ion can be

readily to occupy the Ti^{4+} lattice site because it has a relatively closer ionic size to Ti than the reported Er, Bi and In ions. Furthermore, a small shifting to low diffraction angle appears with the increasing doping content. It is ascribed to the occupation of Zr^{4+} and Nb^{5+} at the Ti^{4+} sites, leading to a larger cell volume due to lattice expansion.

Fig. 2 presents the Raman results of $\text{Zr}_x\text{Nb}_{0.005}\text{Ti}_{0.995-x}\text{O}_2$ ceramics ($x = 0\%, 0.5\%, 2\%, 5\%$), measured in the range of $100\sim 1000\text{ cm}^{-1}$. The B_{1g} , E_g , A_{1g} , and B_{2g} modes are the four Raman active fundamental modes of rutile TiO_2 , locating at $143, 445, 613,$ and 826 cm^{-1} , respectively.⁷ The B_{1g} , E_g and A_{1g} modes are observed in all samples, which indicates the formation of the rutile phase. Meanwhile, the existence of the 239 cm^{-1} peak is ascribed to second-order effect (SOE) which results in such a multi-phonon peak.³² It is generally accepted that the peak is associated with the internal strain and partial reduction of the TiO_2 grains induced by impurity doping into the host lattice. Moreover, there is no extra Raman information in Fig. 2. It suggests the formation of pure rutile TiO_2 for the co-doped samples, which is compatible with the analysis of XRD patterns. The Raman peaks exhibit red shift, asymmetric low-frequency broadening, and decrease in Raman intensity with the increasing doping level. For example, the E_g Raman peak shifts from 447 cm^{-1} to 440.6 cm^{-1} and the peak intensity reduces by half when the doping content is increased to 5%. Raman shift could be sensitive to the effect of oxygen vacancies or grain size.^{12,32} The Raman peaks of $(\text{Mg}_{1/3}\text{Nb}_{2/3})_x\text{Ti}_{1-x}\text{O}_2$ ceramics also exhibited the red shift, asymmetric low-frequency broadening, and decrease in the peak height-to-half-width ratio as x increased. The change might be induced by decreasing crystallite size not by oxygen content because the oxygen content should be the same theoretically. Therefore, we think that the possible main cause for this observation is the reduction of grain size.

As shown in Fig. 3, we investigated the evolution of the surface morphologies of the co-doped

ceramics by SEM technique. All of the characterized ceramics are clearly observed to possess a dense microstructure. A bi-modal size distribution can be found with larger coarse grains surrounded by smaller fine grains in all samples. The size of larger grains shows a gradual decrease from about 13 μm to 8 μm with the increasing doping concentrations from 0.5% to 2% but that of smaller ones remains stable at about 5 μm for the co-doped samples. Remarkably, grain size is almost unchanged when the doping level exceeded 2%. The grain size decreased with the increase of Zr doping level, which may be related to the liquid phase sintering mechanism. Normally, the grain growth of a polycrystalline ceramics is caused by mass transport across the grain boundary by diffusion of ions or atoms.⁹ It would result in the movement of the grain boundary. On the heating process, if the liquid phase in the ceramic microstructure was formed, it can enhance the diffusion rate of ions.⁹ This leads to a large enhancement of the grain boundary mobility.⁹ However, the Zr dopant in our work might inhibit the formation of liquid phase and then drag the grain boundary mobility, resulting in the decrease of grain size. It is similar to the results in (Yb+Nb) co-doped TiO_2 ,¹⁹ Zr doped SrTiO_3 ²⁷ and (Ga+Ta) co-doped TiO_2 .³⁴ To clarify the elemental composition and distributions of the (Zr+Nb) co-doped TiO_2 , partial element mapping was carried out as presented in Fig. 4. This result indicates that the elements Nb, Zr, Ti, and O are homogeneously distributed across the grains and grain boundaries and there is no second phase in the co-doped TiO_2 ceramics.

Dielectric properties at room temperature of $\text{Zr}_x\text{Nb}_{0.005}\text{Ti}_{0.995-x}\text{O}_2$ ceramics are given as a function of measuring frequencies in Fig. 5. There is almost no influence on the permittivity by doping only with Zr in the host TiO_2 , which is similar to the reported doping only with acceptor elements (In, Er and Mg) in TiO_2 .^{1,14,18} By contrast, doping with Nb only significantly increases the permittivity up to about 3×10^4 by two orders. Unfortunately, the $\tan \delta$ is mostly over 0.1 in the measuring frequency

range. For the co-doped samples, it is found that the dielectric loss can be reduced greatly while the CP can be maintained. For example, a relatively low dielectric loss (mostly < 0.1) at room temperature was obtained for the doping level of $x = 2\%$ and $x = 5\%$ from 10^2 Hz $\sim 10^6$ Hz, as shown in Fig. 3(a). Especially, the CP of 4×10^4 as well as the lowest dielectric loss (0.018) is found at 7 kHz for the $x = 2\%$ sample. The loss of the 2% doped sample is lower than 0.05 from 300 Hz to 10^5 Hz. Therefore, Zr co-doping not only reduces the dielectric loss, but also effectively improves the frequency stability for the CP properties of single Nb doped TiO_2 which exhibits a high strong frequency dependence of the dielectric loss.³⁵ In addition, the temperature dependence of the dielectric properties of the doped sample ($x = 5\%$) was recorded at 1 kHz, 5 kHz and 100 kHz in the temperature range from room temperature to 490 °C, as shown in Fig. 6. An enlargement of the temperature zone $0 < T < 200$ °C about the dielectric properties is depicted in the inset of Fig. 6. It can be seen that the high permittivity and low loss are kept stable from room temperature to around 100 °C. But both of them gradually increase when the measured temperature exceeds 100 °C.

In order to explain the CP properties of (Zr+Nb) co-doped TiO_2 ceramics and explore their underlying mechanism, we also carry out the XPS analysis. Fig. 7 compares the XPS results of 0.5% and 5% doped samples. The Nb 3d profiles for the sample of $x = 0.5\%$ and 10% are shown in Fig. 7(a). The two peaks of 206.9 eV and 209.6 eV are observed for Nb $3d_{5/2}$ and Nb $3d_{3/2}$, respectively. The spacing of 2.7 eV is caused by the spin-orbit splitting, which is consistent with that of reported co-doped TiO_2 .^{14,18,36} Besides, no extra Nb 3d information from other valence states with low binding energy is found. It reveals only one Nb 3d chemical environment with the oxidation state of +5 in the ceramic.³⁷ Fig. 7(b) shows the XPS of Zr elements in (Zr+Nb) co-doped TiO_2 ceramics. The binding energies of Zr 3d electrons are 181.8 eV and 184.2 eV, respectively, for $3d_{5/2}$ and $3d_{3/2}$, implying an

oxidation state of +4 for Zr. In other words, the valance states of Nb and Zr ions are stable regardless of doping concentration. In addition, the binding energies of the Ti 2p with 2p_{3/2} and 2p_{1/2} are 458.4 eV and 464.2 eV, respectively. Ti³⁺ signals are also detected with a low concentration. The partial reduction of Ti⁴⁺ to Ti³⁺ can be explained by the introduction of Nb⁵⁺ as: $\text{Nb}_2\text{O}_5 + 2\text{TiO}_2 \xrightarrow{4\text{TiO}_2} 2\text{Nb}_{\text{Ti}}^{\bullet} + 2\text{Ti}'_{\text{Ti}} + 8\text{O}_\text{O} + 1/2\text{O}_2$ and $\text{Ti}^{4+} + e \rightarrow \text{Ti}^{3+}$. The percentages of Ti³⁺ at the doping level of $x = 0.5\%$ and 5% have almost no obvious change. The O 1s peaks showed in Fig. 7(d) can be fitted by three components: bulk Ti–O, oxygen vacancies, and adsorbed surface H₂O. The binding energies of them correspond to 529.8 eV, 530.9 (531.2) eV, 531.7 (532.7) eV, respectively. Interestingly, the concentration of oxygen vacancies decreases evidently as x is increased from 0.5% to 5%, which could be explained as: $\text{ZrO}_2 + 2\text{V}_\text{O}^{\bullet\bullet} \xrightarrow{\text{TiO}_2} \text{Zr}_{\text{Ti}} + 2\text{O}_\text{O}$.³⁸ The limited Ti³⁺ and partial oxygen vacancies could form the complex defect dipoles. Therefore, the improved dielectric performance could be attributed to the complex defect dipoles and a small amount of oxygen vacancies.

The technique of complex impedance spectra (Cole-Cole plot) is used for distinguishing the intrinsic (bulk) properties from the extrinsic contributions such as grain boundaries, surface layers, and electrode contacts.³⁹ As shown in Fig. 8(a), it presents the high temperature complex impedance (130 °C ~ 230 °C) for $x = 5\%$ sample which can be well fitted by a RC model. According to the RC model, it consists of a bulk resistance and capacitance. The semicircle indicates the dominance of grain effect on the grain boundary.⁴⁰ At the same time, the temperature-dependent grain conductivity (σ_g) can generally be described as $\ln \sigma_g \sim T^{-S}$, with $S = 1$ for Arrhenius type nearest neighbour hopping, as shown in Fig. 8(b). The conductive activation energy of the 0.5% doped sample calculated from the impedance spectra is 0.668 eV. A higher conductive activation energy of 0.873 eV is found for the 5% doped sample. Similarly, the temperature-variation of conductivity of the (Al+Nb) or (Ga+Ta) co-

doped TiO₂ also obeys the Arrhenius law.^{10,34} It is different from the Mott-VRH behavior in the case of only Nb-doped TiO₂.¹ Both of them thought that the CP mechanism could be attributed to the IBLC effect which can be excluded because of the direct current (DC) bias stress-independent capacitance in this work. Therefore, we can speculate that it might be contributed from the existence of the giant defect dipoles associated with oxygen vacancies in the bulk based on our XPS results.²⁷ With the increase in oxygen vacancies concentration, the correlation among the oxygen vacancies strengthens, and thus the movement of oxygen vacancies becomes easier and the activation energy decreases.⁴¹ Otherwise, the activation energy will increase with the decrease of oxygen vacancies concentration. In our work, the oxygen vacancies concentration decreased with the increase of Zr doping level from 2% to 5%. It means that the Zr doping can promote the conductive activation energy of the ceramics by inhibiting the formation of the oxygen vacancies, and thus lower dielectric loss of Nb-doped TiO₂.

Moreover, we measured the dielectric properties under an applied DC bias to explore the possibility of the IBLC effect, as shown in Fig. 9. The permittivity remains nearly unchanged under DC biases and after withdrawal of the DC bias in the measuring frequencies range. It is similar to those systems following the EPDD mechanism.¹⁷ Conversely, the dielectric properties would be dependent on applied DC bias in (Sc+Nb), (Ga+Ta) co-doped systems based on IBLC effect.^{34,42} In such interfacial polarization dominated systems, numerous space charges are accumulated at interfacial region, resulting in significant increase of permittivity and dielectric loss when a small DC bias is applied.^{22,43,44} Therefore, we can speculate that the IBLC effect is not the main reason for the high permittivity and the low loss in Zr+Nb co-doped TiO₂ ceramics. According to EPDD model, local defect clusters were proposed to explain the observed excellent dielectric behavior in In+Nb co-doped TiO₂ ceramics.¹ The acceptor In³⁺ ions induce the formation of oxygen vacancies for charge

compensation. Oxygen vacancies would be also formed at high temperature sintering in this work, which can be confirmed by XPS analysis. But the oxygen vacancies concentration can be suppressed by the doping of Zr ions into Ti sites.³⁸ Moreover, the electron produced by Nb doping would be also localized in the defect clusters related to the oxygen vacancies, like $\{ \text{Ti}^{4+} \bullet e - V_{\text{O}}^{\bullet\bullet} - \text{Ti}^{4+} \bullet e \}$.²⁷ Therefore, it is considered that the Zr doping could improve the dielectric properties of co-doped TiO₂ ceramics according to the defect clusters associated with oxygen vacancies.

4. Conclusions

In this work, the contributions of isovalent Zr doping on the CP properties of (Zr+Nb) co-doped rutile TiO₂ are investigated. With the increase of Zr doping content, the grain size decreases and then remains almost unchanged when the Zr doping content is increased up to 2%. Dielectric loss gradually decreases with increasing Zr doping concentration. An acceptable frequency- and temperature-independence is showed in the co-doped CP ceramics. Especially, a low dielectric loss is 0.029 and a high ϵ_r is 6.4×10^4 , for $x = 2\%$ sample measured at room temperature and 1 kHz. Based on the analysis of XPS and the impedance spectra, the improving dielectric properties can be ascribed to the existence of defect dipoles related to oxygen vacancies. The results will provide a new routine to achieve a low dielectric loss in the CP materials through incorporating into a stable isovalent ion.

Acknowledgment

The authors are thankful to Prof. Dunmin Lin (Sichuan Normal University) during the dielectric measurements at high temperature for technical support and useful discussion. This work has been supported by the Open Project of the State Key Laboratory Cultivation Base for Nonmetal Composites and Functional Materials (No. 11zxfk17) and Program for Young Science and Technology Innovation Team of Sichuan Province (2017TD0020). J. H. acknowledges financial support from the grant

Research Grants Council of Hong Kong (GRF No. PolyU 153004/14P).

References

1. Hu WB, Liu Y, Withers RL, Frankcombe TJ, Norén L, Snashall A, Kitchin M, Smith P, Gong B, Chen H, Schiemer J, Brink F, Wong-Leung J. Electron-pinned defect-dipoles for high-performance colossal permittivity materials. *Nature Mater.* 2013;12:821-826.
2. Buscaglia MT, Viviani M, Buscaglia V, Mitoseriu L, Testino A, Nanni P, Zhao Z, Nygren M, Harnagea C, Piazza D, Galassi C. High dielectric constant and frozen macroscopic polarization in dense nanocrystalline BaTiO₃ ceramics. *Phys Rev B.* 2006;73:064114.
3. Fang TT, Shiau HK. Mechanism for developing the boundary barrier layers of CaCu₃Ti₄O₁₂. *J Am Ceram Soc.* 2004;87:2072-2079.
4. Homes CC, Vogt T, Shapiro SM, Wakimoto S, Ramirez AP. Optical response of high-dielectric-constant perovskite-related oxide. *Science.* 2001;293:673-676.
5. Wu JB, Nan CW, Lin YH, Deng Y. Giant dielectric permittivity observed in Li and Ti doped NiO. *Phys Rev Lett.* 2002; 89:217601.
6. Krohns S, Lunkenheimer P, Kant Ch, Pronin AV, Brom HB, Nugroho AA, Diantoro M, Loidl A. Colossal dielectric constant up to gigahertz at room temperature. *Appl Phys Lett.* 2009;94:122903.
7. Cheng XJ, Li ZW, Wu JG. Colossal permittivity in ceramics of TiO₂ co-doped with niobium and trivalent cation. *J Mater Chem A.* 2015;3:5805-5810.
8. Li ZW, Wu JG, Xiao DQ, Zhu JG, Wu WJ. Colossal permittivity in titanium dioxide ceramics modified by tantalum and trivalent elements. *Acta Mater.* 2016;103:243-251.
9. Tuichai W, Srepusharawoot P, Swatsitang E, Danwittayakuld S, Thongbai P. Giant dielectric permittivity and electronic structure in (Al+Sb) co-doped TiO₂ ceramics. *Microelectron Eng.* 2015;146:32-37.

10. Song YL, Wang XJ, Zhang XQ, Sui Y, Zhang Y, Liu ZG, Lv Z, Wang Y, Xu P, Song B. The contribution of doped-Al on the colossal permittivity properties of $\text{Al}_x\text{Nb}_{0.03}\text{Ti}_{0.97-x}\text{O}_2$ rutile ceramics. *J Mater Chem C*. 2016;4:6798-6805.
11. Dong W, Hu WB, Berlie A, Lau K, Chen H, Withers RL, Liu Y. Colossal dielectric behavior of Ga+Nb co-doped rutile TiO_2 . *ACS Appl Mater Interfaces*. 2015;7: 25321-25325.
12. Hu WB, Lau K, Liu Y, Withers RL, Chen H, Fu L, Gong B, Hutchison W. Colossal dielectric permittivity in (Nb+Al) codoped rutile TiO_2 ceramics: compositional gradient and local structure. *Chem Mater*. 2015;27:4934-4942.
13. Tse MY, Tsang MK, Wong YT, Chan YL, Hao JH. Simultaneous observation of up/down conversion photoluminescence and colossal permittivity properties in (Er+Nb) co-doped TiO_2 materials. *Appl Phys Lett*. 2016;109:042903.
14. Tse MY, Wei XH, Hao JH. High-performance colossal permittivity materials of (Nb+Er) co-doped TiO_2 for large capacitors and high-energy-density storage devices. *Phys Chem Chem Phys*. 2016;18:24270-24277.
15. Li ZW, Wu JG, Wu WJ. Composition dependence of colossal permittivity in $(\text{Sm}_{0.5}\text{Ta}_{0.5})_x\text{Ti}_{1-x}\text{O}_2$ ceramics. *J Mater Chem C*. 2015;3:9206-9216.
16. Wei XH, Jie WJ, Yang ZB, Zheng FG, Zeng HZ, Liu Y, Hao JH. Colossal permittivity properties of Zn, Nb co-doped TiO_2 with different phase structures. *J Mater Chem C*. 2015;3:11005-11010.
17. Dong W, Hu WB, Frankcombe T, Chen DH, Zhou C, Fu ZX, Cândido L, Hai GQ, Chen H, Li YX, Withers R, Liu Y. Colossal permittivity with ultralow dielectric loss in In+Ta co-doped rutile TiO_2 . *J Mater Chem A*. 2017;5:5436-5441.
18. Yang C, Tse MY, Wei XH, Hao JH. Colossal permittivity of (Mg+Nb) co-doped TiO_2 ceramics

with low dielectric loss. *J Mater Chem C*. 2017;5:5170-5175.

19. Zhao XG, Liu P. Dielectric and electric relaxations induced by the complex defect clusters in (Yb+Nb) co-doped rutile TiO₂ ceramics. *J Am Ceram Soc*. 2017;100:3505-3513.

20. Li ZW, Luo X, Wu WJ, Wu JG. Niobium and Divalent-Modified Titanium Dioxide Ceramics: Colossal Permittivity and Composition Design. *J Am Ceram Soc*. 2017;100:3004-3012.

21. Nachaithong T, Tuichai W, Kidkhunthod P, Chanlek N, Thongbai P, Maensiri S. Preparation, characterization, and giant dielectric permittivity of (Y³⁺ and Nb⁵⁺) co-doped TiO₂ ceramics. *J Eur Ceram Soc*. 2017;37:3521-3526.

22. Li JL, Li F, Li C, Yang G, Xu Z, Zhang SJ. Evidences of grain boundary capacitance effect on the colossal dielectric permittivity in (Nb+In) co-doped TiO₂ ceramics. *Sci Rep*. 2015;5:8295.

23. Zhao XG, Liu P, Song YC, Zhang AP, Chen XM, Zhou JP. Origin of colossal permittivity in (In_{1/2}Nb_{1/2})TiO₂ via broadband dielectric spectroscopy. *Phys Chem Chem Phys*. 2015;17:23132.

24. Nachaithong T, Kidkhunthod P, Thongbai P, Maensiri S. Surface barrier layer effect in (In+ Nb) co-doped TiO₂ ceramics: An alternative route to design low dielectric loss. *J Am Ceram Soc*. 2017;100:1452-1459.

25. Mandal S, Pal S, Kundu AK, Menon KSR, Hazarika A, Rioult M, Belkhou R. Direct view at colossal permittivity in donor-acceptor (Nb, In) co-doped rutile TiO₂. *Appl Phys Lett*. 2016;109:092906.

26. Hume-Rothery W, Smallman RE, Haworth CW. The structure of metals and alloys. *The Institute of Metals*. 1969.

27. Wang ZJ, Cao MH, Zhang Q, Hao H, Yao ZH, Wang ZH, Song Z, Zhang YM, Hu W, Liu HX. Dielectric Relaxation in Zr-Doped SrTiO₃ Ceramics Sintered in N₂ with Giant Permittivity and Low Dielectric Loss. *J Am Ceram Soc*. 2015;98:476-482.

28. Yakovlev S, Yoo C-Y, Fang S, Bouwmeester HJM. Phase transformation and oxygen equilibration kinetics of pure and Zr-doped $\text{Ba}_{0.5}\text{Sr}_{0.5}\text{Co}_{0.8}\text{Fe}_{0.2}\text{O}_{3-\delta}$ perovskite oxide probed by electrical conductivity relaxation. *Appl Phys Lett*. 2010;96:254101.
29. Jesurani S, Kanagesan S, Hashim M, Ismail I. Dielectric properties of Zr doped $\text{CaCu}_3\text{Ti}_4\text{O}_{12}$ synthesized by sol-gel route. *J Alloys Compd*. 2013;551:456-462.
30. Cancarevic M, Zinkevich M, Aldinger F. Thermodynamic assessment of the PZT system. *J Ceram Soc Jpn*. 2006;114:937-949.
31. Troitzsch U, Ellis DJ. The ZrO_2 - TiO_2 phase diagram. *J Mater Sci*. 2005;40:4571-4577.
32. Swamy V, Muddle BC, Dai Q. Size-dependent modifications of the Raman spectrum of rutile TiO_2 . *Appl Phys Lett*. 2006;89:163118.
33. Li JL, L F, Zhuang YY, L J, Wang LH, Wei XY, Xu Z, Zhang SJ. Microstructure and dielectric properties of (Nb + In) co-doped rutile TiO_2 ceramics. *J Appl Phys*. 2014;116:074105.
34. Tuichai W, Thongyong N, Danwittayakul S, Chanlek N, Srepusharawoot P, Thongbai P, Maensiri S. Very low dielectric loss and giant dielectric response with excellent temperature stability of Ga^{3+} and Ta^{5+} co-doped rutile- TiO_2 ceramics. *Mater Des*. 2017;123:15-23.
35. Li FC, Shang BQ, Liang PF, Wei LL, Yang ZP. Defect Complex Effect in Nb Doped TiO_2 Ceramics with Colossal Permittivity. *J Electron Mater*. 2016;45:5178-5184.
36. Han HS, Dufour P, Mhin S, Ryu JH, Tenailleau C, Guillemet-Fritsch S. Quasi-intrinsic colossal permittivity in Nb and In co-doped rutile TiO_2 nanoceramics synthesized through a oxalate chemical-solution route combined with spark plasma sintering. *Phys Chem Chem Phys*. 2015;17: 16864-16875.

37. Morris D, Dou Y, Rebane J, Mitchell CEJ, Egdell RG, Law DSL, Vittadini A, Casarin M. Photoemission and STM study of the electronic structure of Nb-doped TiO₂. *Phys Rev B* 2000;61:13445.
38. Chi QG, Gao L, Wang X, Lin JQ, Sun J, Lei QQ. Effects of Zr doping on the microstructures and dielectric properties of CaCu₃Ti₄O₁₂ ceramics. *J Alloys Compd.* 2013;559:45-48.
39. Li M, Feteira A, Sinclair DC. Origin of the high permittivity in (La_{0.4}Ba_{0.4}Ca_{0.2})(Mn_{0.4}Ti_{0.6})O₃ ceramics. *J Appl Phys.* 2005;98:084101.
40. Das R, Sarkar T, Mandal K. Multiferroic properties of Ba²⁺ and Gd³⁺ co-doped bismuth ferrite: magnetic, ferroelectric and impedance spectroscopic analysis. *J Phys D: Appl Phys.* 2012;45:455002.
41. Wang XF, Lu XM, Zhang C, Wu XB, Cai W, Peng S, Bo HF, Kan Y, Huang FZ, Zhu JS. Oxygen-vacancy-related high-temperature dielectric relaxation in SrTiO₃ ceramics. *J Appl Phys.* 2010;107:114101.
42. Tuichai W, Danwittayakul S, Chanlek N, Thongbaiet P, Maensiri S. High-performance giant-dielectric properties of rutile TiO₂ co-doped with acceptor-Sc³⁺ and donor-Nb⁵⁺ ions. *J Alloys Compd.* 2017;703:139-147.
43. Liu GZ, Wang C, Wang CC, Qiu J, He M, Xing J, Jin KJ, Lu HB, Yang GZ. Effects of interfacial polarization on the dielectric properties of BiFeO₃ thin film capacitors. *Appl Phys Lett.* 2008;92:122903.
44. Lunkenheimer P, Fichtl R, Ebbinghaus SG, Loidl A. Nonintrinsic origin of the colossal dielectric constants in CaCu₃Ti₄O₁₂. *Phys Rev B.* 2004;70:172102.

Figure captions

FIG. 1. (a) XRD patterns of $Zr_xNb_{0.005}Ti_{0.995-x}O_2$, 0.5% only Zr-doped TiO_2 , and pure TiO_2 ceramics, (b) An enlargement 2θ zone comparing the intermediate phases and rutile phase.

FIG. 2. Raman spectra of $Zr_xNb_{0.005}Ti_{0.995-x}O_2$, 0.5% only Zr-doped TiO_2 , and pure TiO_2 ceramics.

FIG. 3. Surface morphologies of $Zr_xNb_{0.005}Ti_{0.995-x}O_2$ ceramics with doping contents of $x = 0\%$ (a), 0.5% (b), 2% (c) and 5% (d).

FIG. 4. Elements mapping of $x = 2\%$ doped ceramics: (a) O, (b) Zr, (c) Nb, and (d) Ti.

FIG. 5. Frequency-dependence (room temperature) of dielectric properties for $Zr_xNb_{0.005}Ti_{0.995-x}O_2$, 0.5% only Zr-doped TiO_2 , and pure TiO_2 ceramics.

FIG. 6. Temperature-dependence of dielectric properties measured at different frequencies for doping concentration of $x = 5\%$ doped sample, an enlargement of the temperature zone $0 < T < 200$ °C about the dielectric properties shown in the inset.

FIG. 7. Valence states of the elements in $x = 0.5\%$ and $x = 5\%$ doped TiO_2 : (a) Nb 3d, (b) Zr 3d, (c) Ti 2p, and (d) O 1s.

FIG. 8. (a) Complex impedance plots [$Z'(\omega)$ - $Z''(\omega)$] (open dots) of $x = 5\%$ doped TiO_2 measured from 130 °C to 230 °C, and corresponding fitting results (solid lines) using a Cole–Cole model, (b) Grain conductivities for $x = 0.5\%$ and $x = 5\%$ doped TiO_2 versus temperature, fitted (solid lines) by Arrhenius.

FIG. 9. Frequency-dependent dielectric properties 0.5% (Zr+Nb) co-doped rutile TiO_2 measured under different DC bias voltage (0.5 V, 5 V and 10 V) and after withdrawal of the DC bias.

Fig. 1

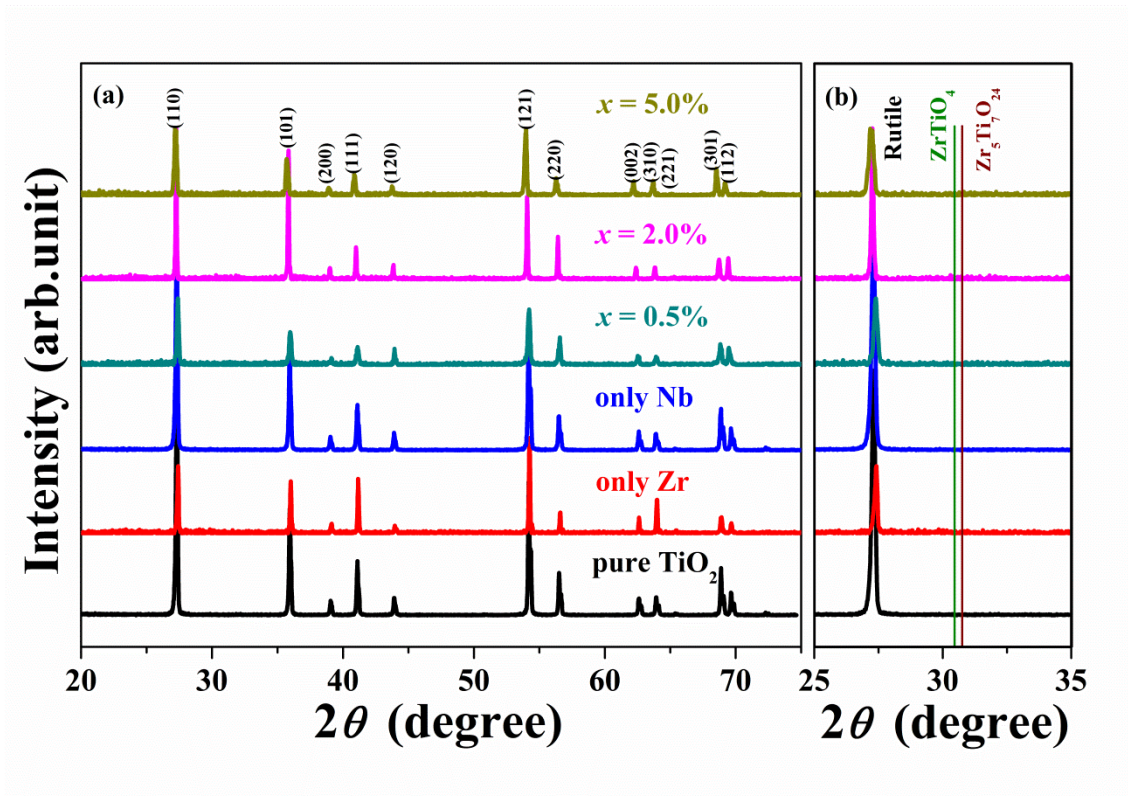


Fig. 2

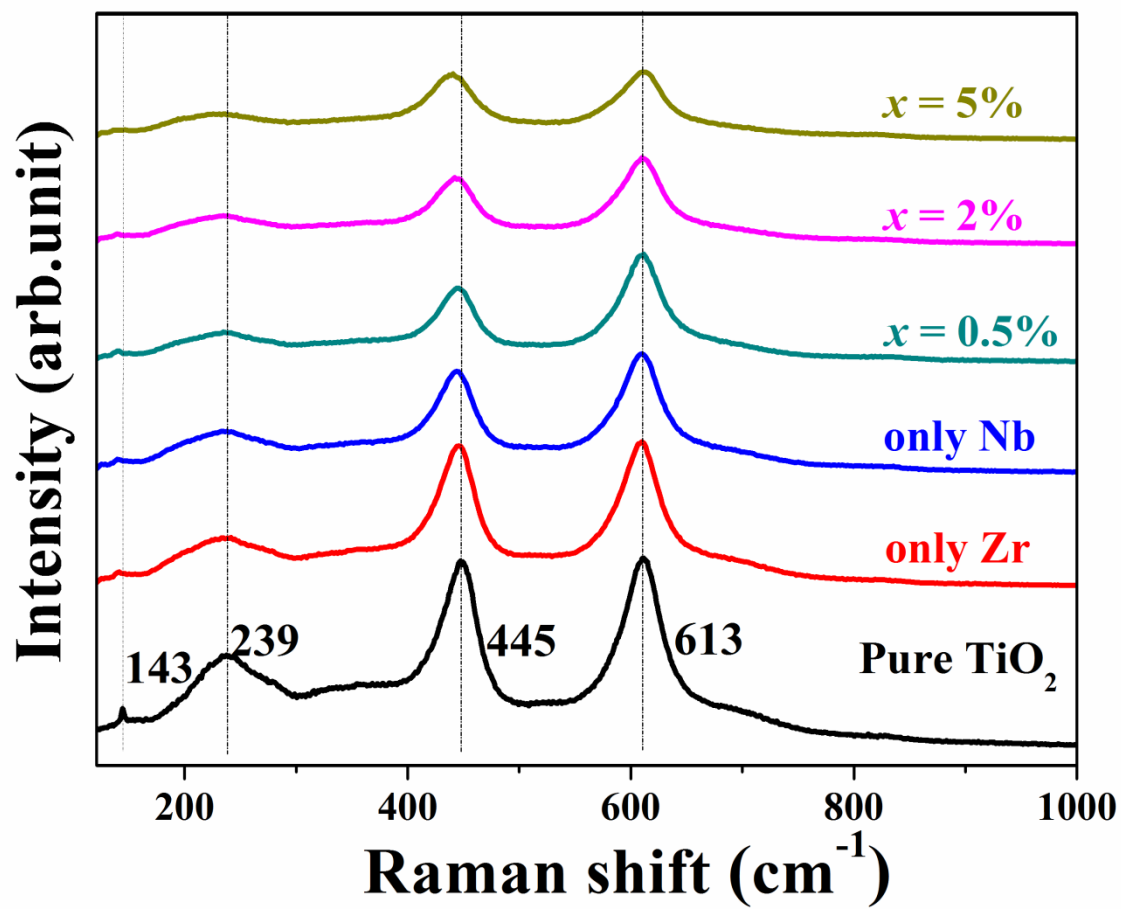


Fig. 3

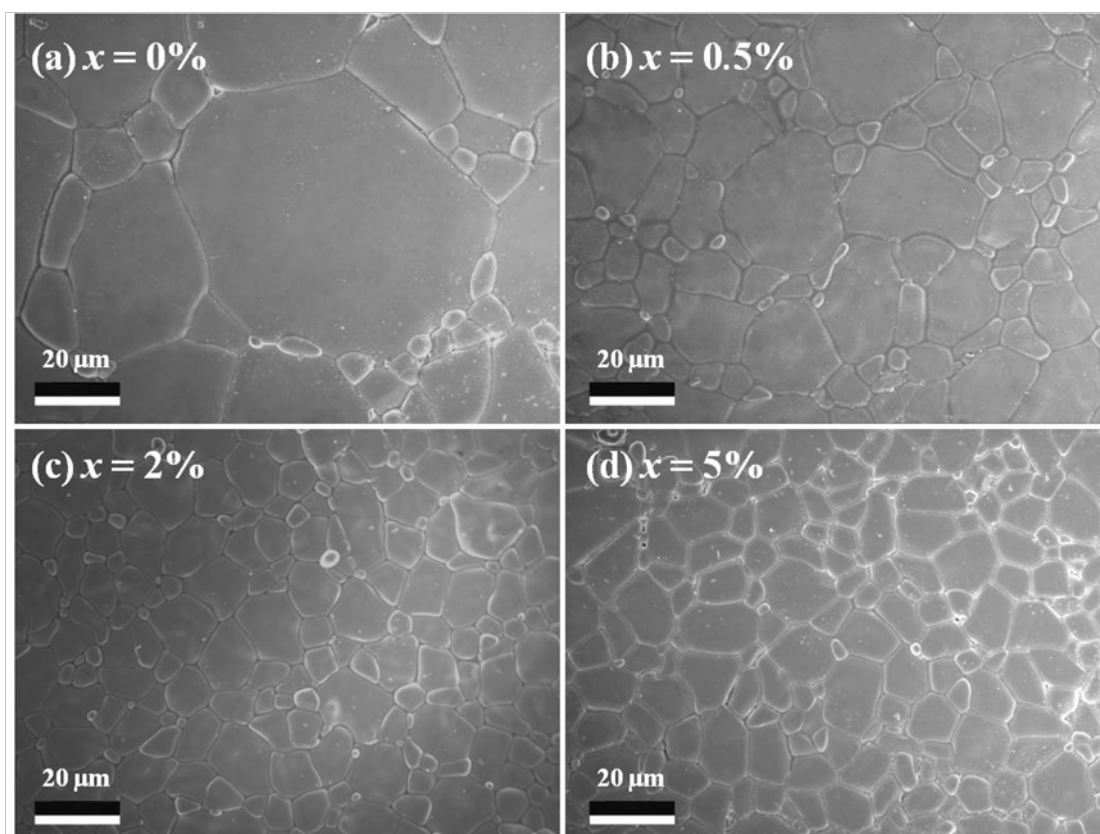


Fig. 4

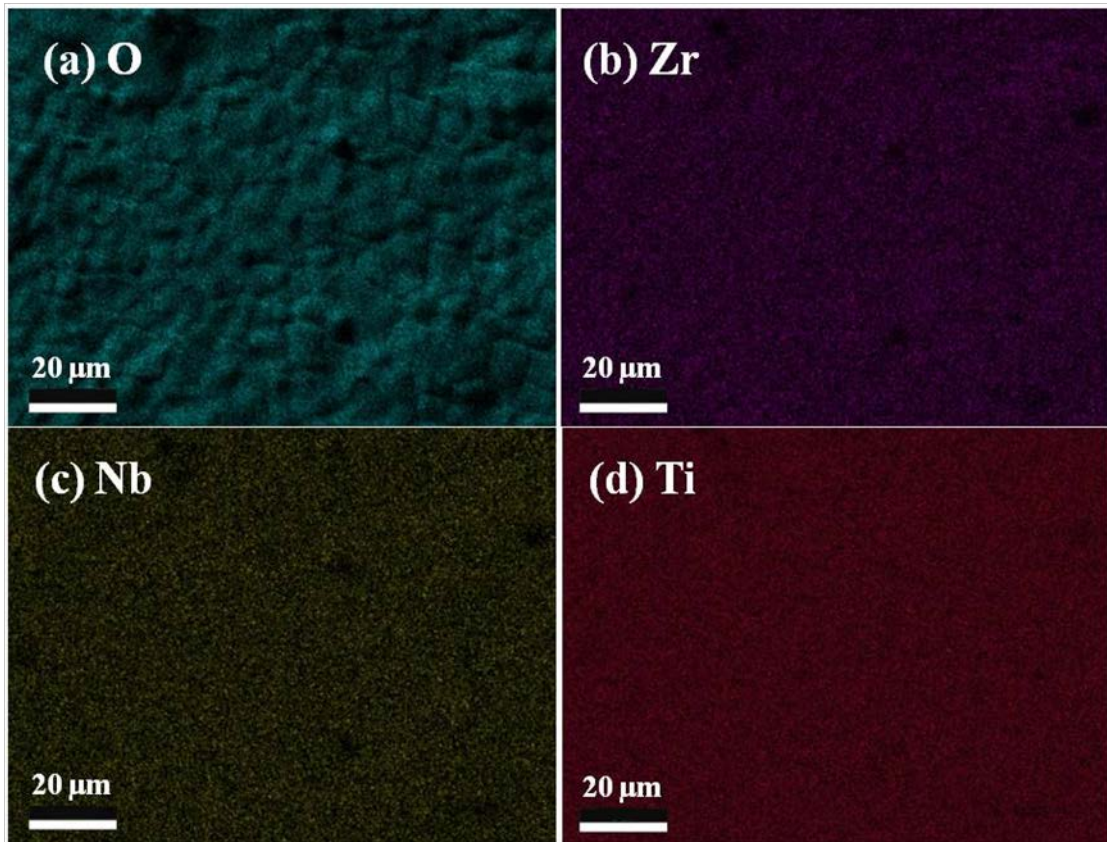


Fig. 5

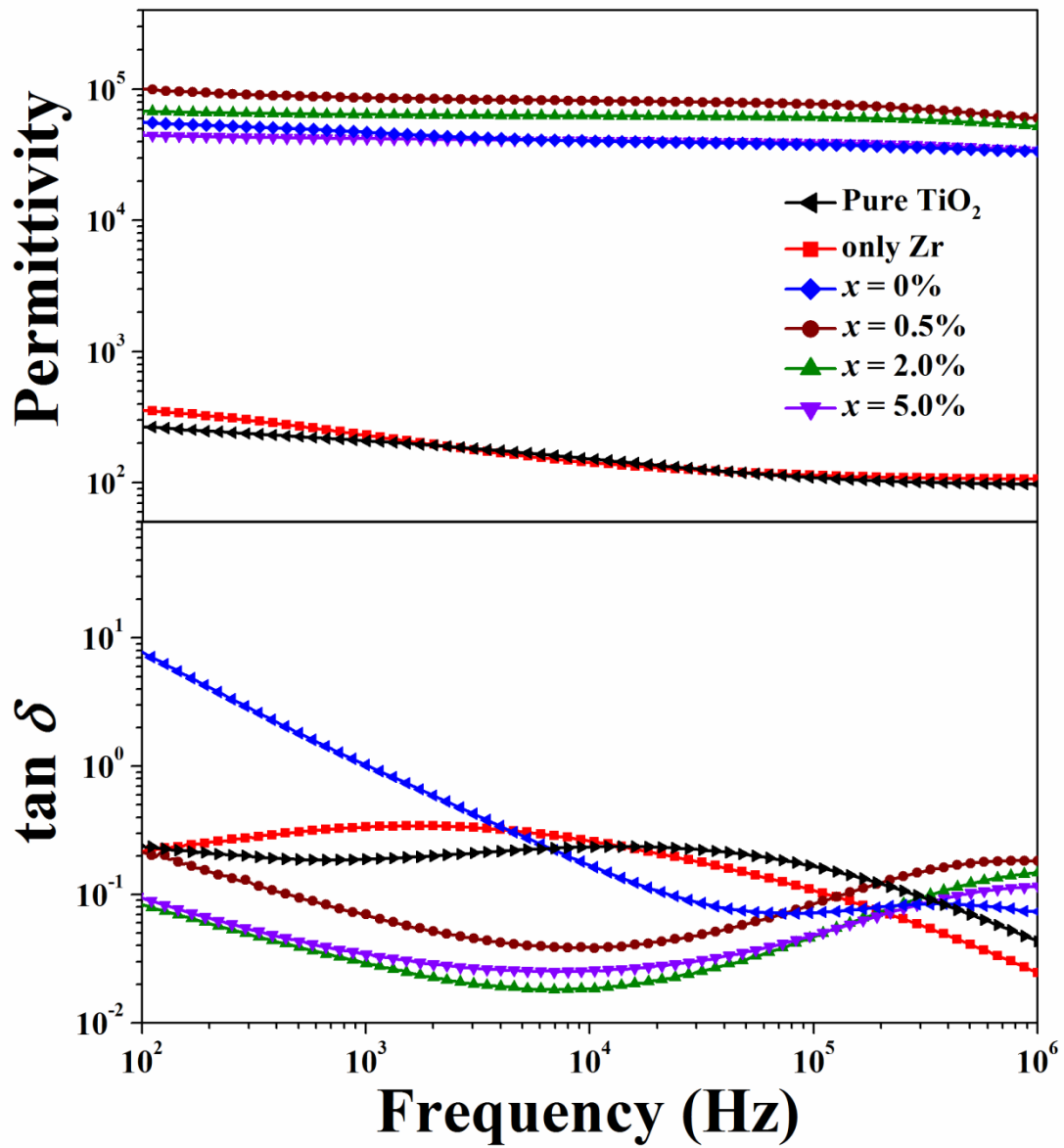


Fig. 6

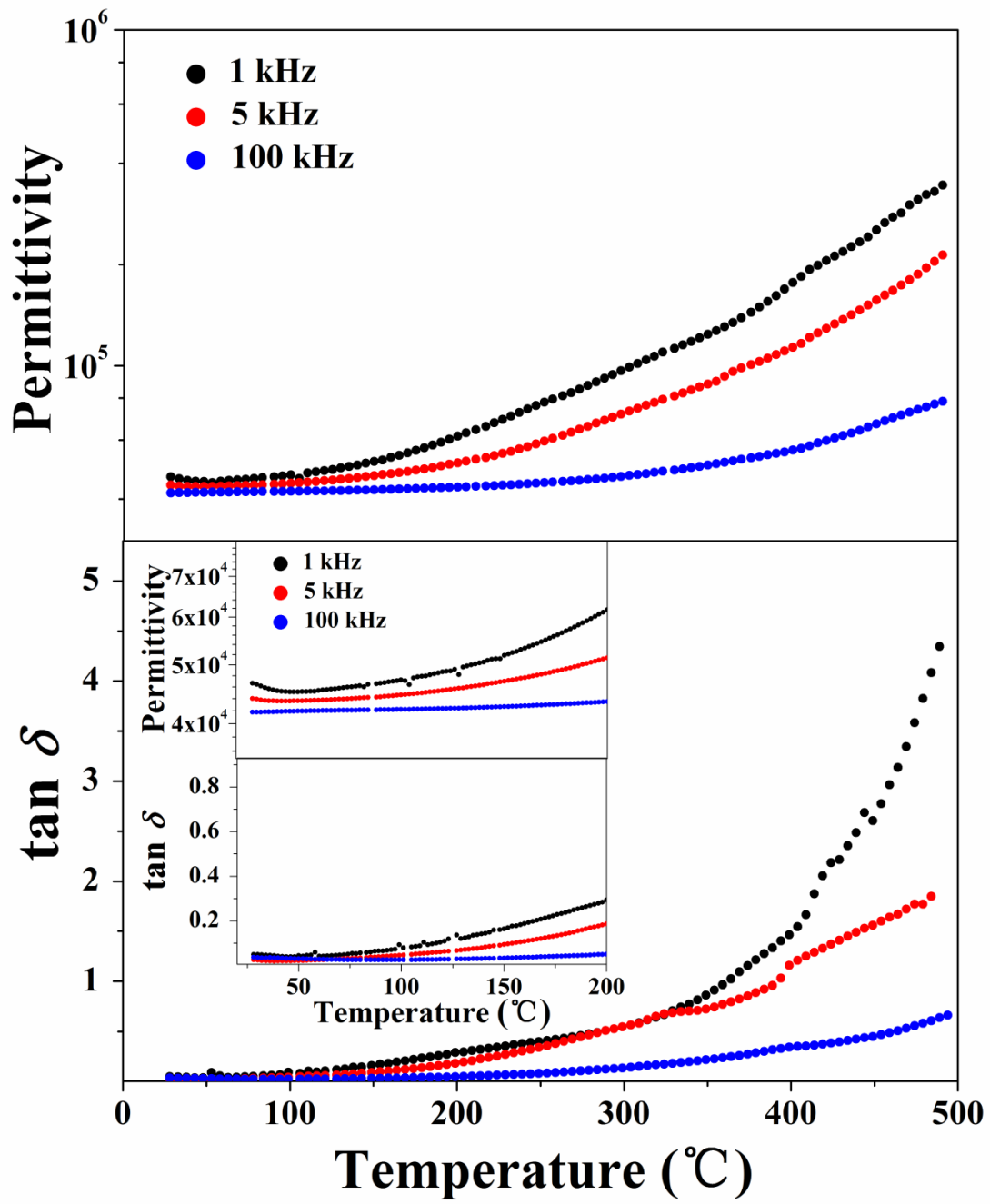


Fig. 7

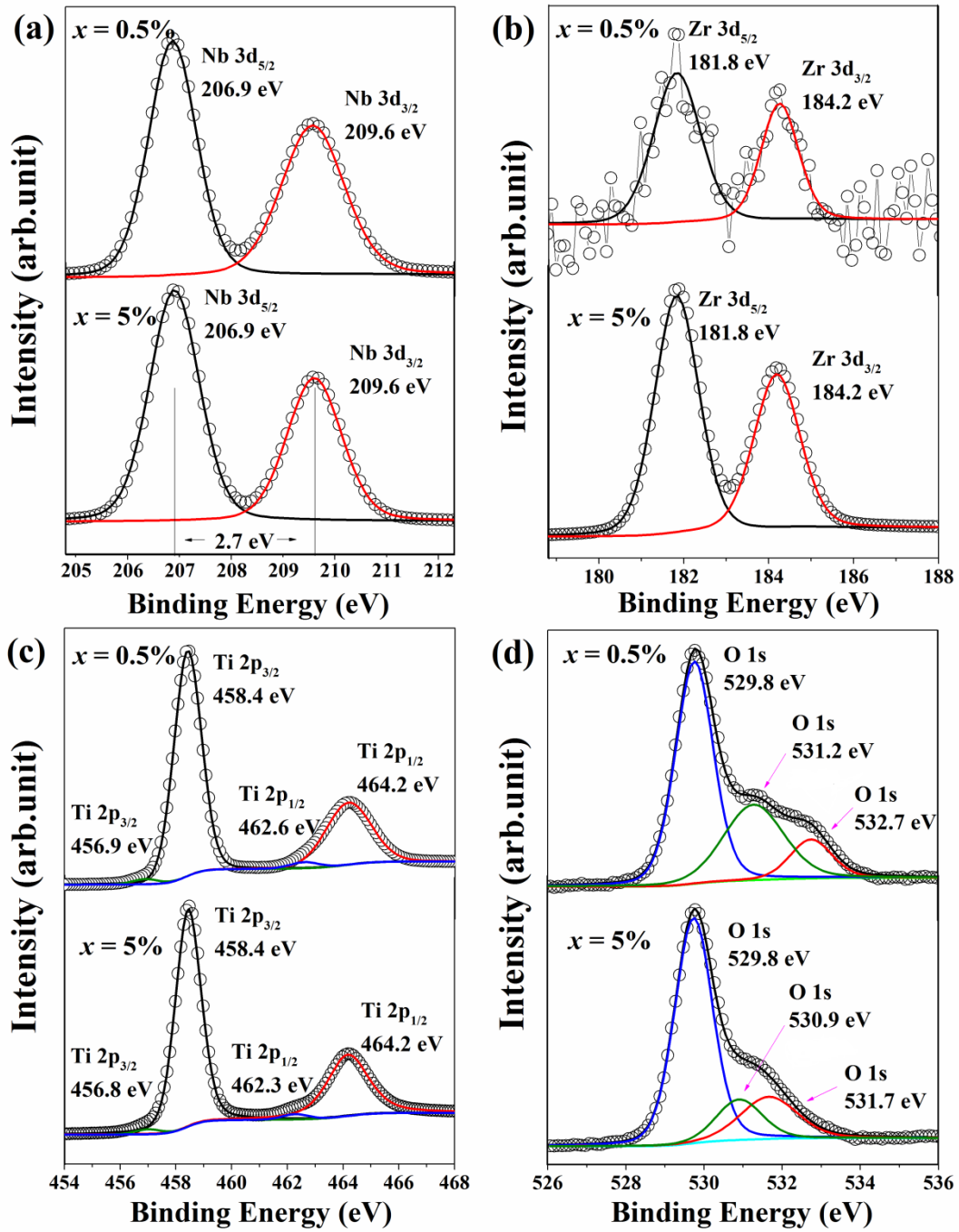


Fig. 8

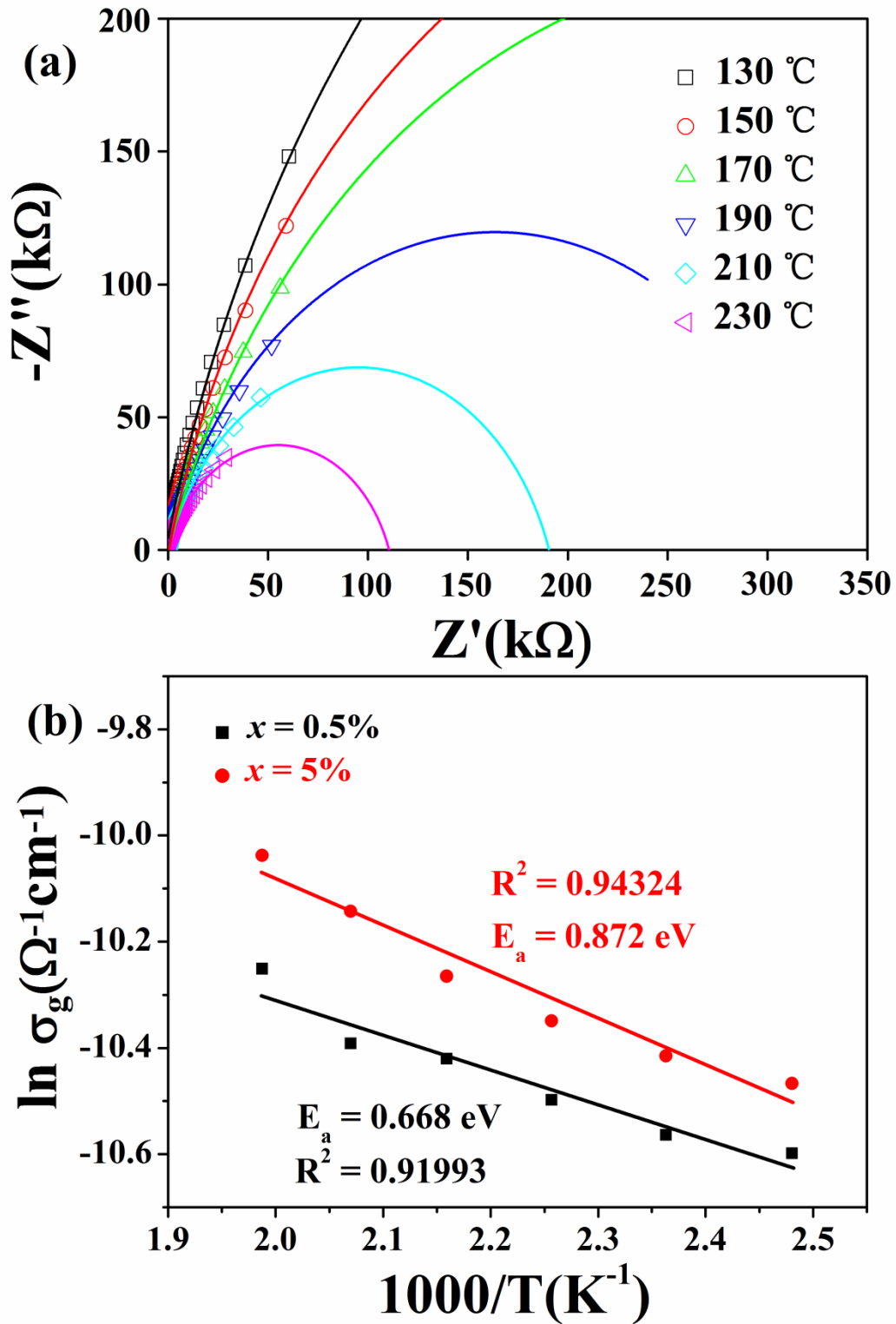


Fig. 9

